

## XRD, FTIR And Electrical Properties Investigation Of Ni<sub>0.6</sub>Zn<sub>0.4</sub>Cr<sub>x</sub>Fe<sub>2-x</sub>O<sub>4</sub> Thin Films

Ied Mohammed Mnawe<sup>1</sup>, M. Y. Hassaan<sup>1</sup>, Osama Mohmaed Hemeda<sup>2</sup>, A.S. Abdel-Moety<sup>1</sup>

<sup>1</sup>Department of physics, Faculty of Science, Al-Azhar University, Cairo, Egypt.

<sup>2</sup>Department of physics, Faculty of Science, Al-Tanta University, Egypt.

---

### Abstract

Nanoparticles of Ni<sub>0.6</sub>Zn<sub>0.4</sub>Cr<sub>x</sub>Fe<sub>2-x</sub>O<sub>4</sub> were prepared and characterized to understand their structural XRD, FTIR and electrical properties such as dc resistivity as a function of temperature. The dielectric constant ( $\epsilon'$ ) and dielectric loss ( $\tan\delta$ ) are also studied as a function of frequency and temperature. It observes the value of dielectric constant is beginning to rise for  $x = 0.2$  and  $0.4$  at  $530\text{k}^\circ$  and for  $x = 0.6$  at  $510\text{k}^\circ$ . Loss coefficient decreases with increased frequency in all the thin film samples except  $x = 0.4$ . Surface morphology and particle orientation have been investigated by TEM and SEM images. It has scientific and technological importance in recent years due to their magnetic properties and wide range of applications especially when the size of the particles approaches to nanometer scale. They have been used for high-frequency transformer cores, rod antennas, and radio-frequency coils. More recently, these are also used in nano-electronic devices, high-speed integrated circuits as well as in biomedical field as contrasting agents used for magnetic resonance imaging (MRI). Spinel ferrites are materials with good magnetic and electronic properties, which depend strongly on the cation distribution among the tetrahedral and octahedral sites.

---

### Introduction

Magnetic materials, particularly nano-sized ferrites, show a significant change in physical, electrical, and magnetic properties in contrast to their bulk counterparts due to their high surface-to-volume ratio of the grains. Ferrite nanoparticles have scientific and technological importance in recent years due to their magnetic properties and wide range of applications especially when the size of the particles approaches to nanometer scale[1,2]. They have been used for high-frequency transformer cores, rod antennas, and radio-frequency coils. More recently, these are also used in nano-electronic devices, high-speed integrated circuits as well as in biomedical field as contrasting agents used for magnetic resonance imaging (MRI). Spinel ferrites are materials with good magnetic and electronic properties, which depend strongly on the cation distribution among the tetrahedral and octahedral sites. Among the spinel ferrites, nanoparticles of Zinc ferrite (ZnFe<sub>2</sub>O<sub>4</sub>) are the potential candidate for various applications such as radar-absorbing materials, gas sensors, photo-catalyst, and electromagnetic wave-absorbing materials. Preparation method and chemical composition play a key role in incurring ferrites with high quality. Sol-gel method is the most useful and attractive technique for the fabrication of ferrite

nanoparticles due to its advantages like good stoichiometric control, the possibility of obtaining ultra-fine particles in the nano-regime with high crystallinity, superior purity, and uniform particle distribution in a relatively short processing time at a very low temperature with simple laboratory equipment. The present study is focused on the synthesis of Zn ferrite by doping with  $\text{Cr}^{3+}$  ions to explore their applicability in nano-devices. Thus with appropriate selection of preparation method and precursors (metal nitrates) single-phase cubic spinel structure Cr–Zn ferrite nanoparticles with enhanced structural and magnetic properties have been fabricated [3,4,5].

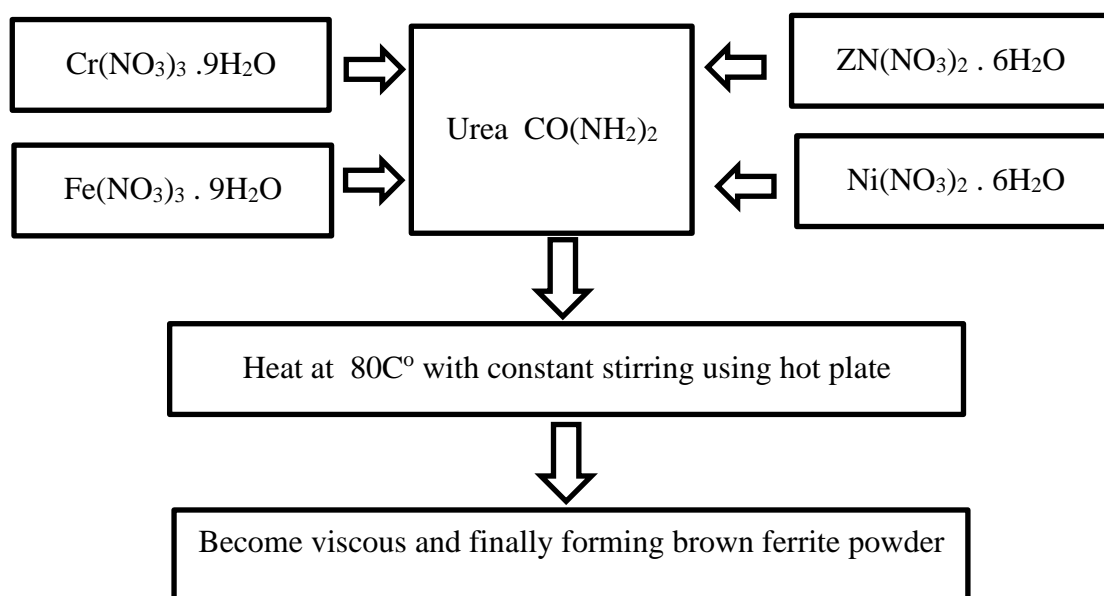
### Experimental producers

#### Samples preparation

The Flash method was applied for the preparation of  $\text{Ni}_{0.6}\text{Zn}_{0.4}\text{Cr}_x\text{Fe}_{2-x}\text{O}_4$ . All chemicals used in this work, including Nickel nitrate  $\text{Ni}(\text{NO}_3)_2$ , Zinc nitrate  $\text{Zn}(\text{NO}_3)_2$ , Chromium nitrate  $\text{Cr}(\text{NO}_3)_3$ , Ferric nitrate  $\text{Fe}(\text{NO}_3)_3$ .

The mixtures of  $\text{Ni Zn Cr Fe}_2\text{O}_4$  firstly prepared and then stirred for 15 minute on hot plate magnetic stirrer, followed with addition of Urea  $\text{CO}(\text{NH}_2)_2$  to the mixtures with stirring. The solutions were evaporated at  $80\text{C}^\circ$  with constant stirring until dryness and then dried in adryer at  $100\text{C}^\circ$  overnight. Thermal analysis of the unannealed precursors was carried. The rate of heating was kept at  $10\text{C}^\circ/\text{min}$  between room temperature and  $800\text{C}^\circ$ . Series perovskite  $\text{Ni}_{0.6}\text{Zn}_{0.4}\text{Cr}_x\text{Fe}_{2-x}\text{O}_4$ ,  $x = (0.0, 0.2, 0.4, 0.6, 0.8 \text{ and } 1)$  was prepared by Flash method as shown in Fig (1-1).

Fig.1. Flow chart for the preparation of samples.



Raw materials of series have been taken in stoichiometric ratios as the following in tables (1)

Tables 1. The weights in grams of  $\text{Ni}_{0.6}\text{Zn}_{0.4}\text{Cr}_x\text{Fe}_{2-x}\text{O}_4$

| Raw materials     |     | Ni(NO <sub>3</sub> ) <sub>2</sub> | Zn(NO <sub>3</sub> ) <sub>2</sub> | Cr(NO <sub>3</sub> ) <sub>3</sub> | Fe <sub>2</sub> O <sub>3</sub> | Total weight |
|-------------------|-----|-----------------------------------|-----------------------------------|-----------------------------------|--------------------------------|--------------|
| Ratios            |     | 0.6                               | 0.4                               | X                                 | 2-x                            |              |
| Molecular weight  |     | 74.709                            | 81.369                            | 68.0001                           | 159.691                        |              |
| X ratio of series | 0.0 | 44.825                            | 32.548                            | 0                                 | 319.382                        | 396.755      |
|                   | 0.2 | 44.825                            | 32.548                            | 13.600                            | 287.443                        | 378.416      |
|                   | 0.4 | 44.825                            | 32.548                            | 27.200                            | 255.506                        | 360.079      |
|                   | 0.6 | 44.825                            | 32.548                            | 40.800                            | 223.567                        | 341.74       |
|                   | 0.8 | 44.825                            | 32.548                            | 54.400                            | 191.629                        | 323.402      |
|                   | 1   | 44.825                            | 32.548                            | 68.0001                           | 159.691                        | 305.064      |

The crushed mass was grinded and pressed as disks and tablets at 5000 kg /cm<sup>2</sup> and sintered at 1200 C° for 2 hours then left to be cooled gradually with the rate 50 C°/ hr.

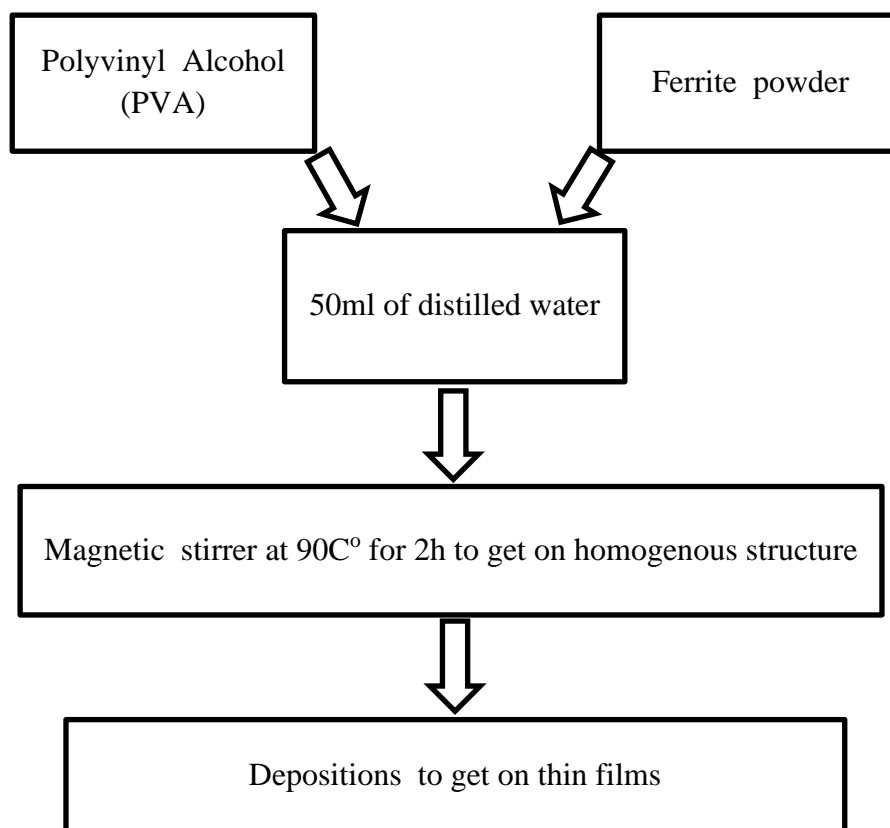
The diameter of the tablets was 1.65 cm and the thickness 0.33 cm for series .

**Fig. 2.** The Compressor



For the purpose of preparing thin films , polyvinyl alcohol was used as a polymeric material (2gm) and was mixed with ferritic powder (0.4gm) , adding 50ml of distilled water to the mixture . It was then placed on the magnetic stirrer at a temperature of 90C° for two hours in order to obtain a homogenous composition , after that the depositions was done and thin films were obtained x = ( 0.0 , 0.2 , 0.4 , 0.6 , 0.8 and 1), as shown in Fig.(3).

**Fig.3.** Flow chart for the preparation of thin films samples .



### Result and discussion

The variation in structural parameters such as crystallite size (D), d-spacing (d) and lattice constant (a) with doping can be explained on the basis of cations size difference that are distributed over sites A and B, whereas site A is smaller in size than site B. Co doping can increase or decrease the value of D, d and a of Ni–Zn ferrite system. It depends on cations distribution in sites A and B having different radii. The value of D, d and a increases, when all Co<sup>2+</sup> ions go to site B in place of Ni<sup>2+</sup> ions.

Using Scherrer's formula (1.1), average crystallite size (D) of all prepared samples has been calculated from full width at half maxima (FWHM)

$$D = 0.9\lambda / \beta \cos\theta \quad (1.1)$$

Where D is the average crystallite size,  $\beta$  is the FWHM of the peak intensity measured in radians,  $\lambda = 1.54 \text{ \AA}$  is the wavelength of x-ray and  $\theta$  is the Bragg's angle. It is found that D initially slightly decreases with Co doping and then increases at high concentration of Co doping ( $x = 0.6$  and  $0.8$ ). This variation has been explained on the basis of cations size difference that is distributed over sites A and B. The slight decrease in D at  $x = 0.0, 0.2$  and  $0.4$  has been expected due to the Co<sup>2+</sup> (ionic radii =  $0.745 \text{ \AA}$ ) and Zn<sup>2+</sup> (ionic radii =  $0.82 \text{ \AA}$ ) ions distribution effect on sites A and B having different radii. Sites B are the most favorable sites for Co<sup>2+</sup> ions occupation. With Co doping at  $x = 0.0, 0.2$  and  $0.4$  in Ni–Zn ferrite, all Co<sup>2+</sup> ions replace Zn<sup>2+</sup> ions at site A and possibly

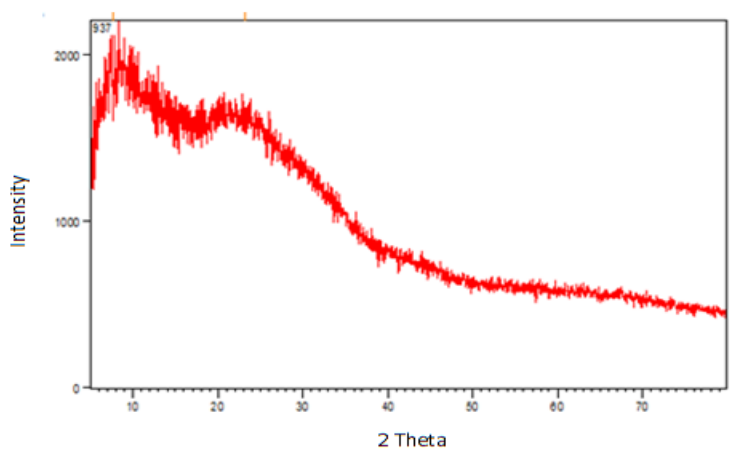
equivalent  $Zn^{2+}$  ions occupy site B in place of  $Ni^{2+}$  (ionic radii =  $0.69 \text{ \AA}$ ) ions. With this type of  $Co^{2+}$  and  $Zn^{2+}$  ions distribution effect, there is slight shrinkage in the unit cell that causes decrease in D. The size obtained at  $x = 0.0$  and  $0.2$  are smaller than the size obtained at  $x = 0.4$  attributed to the presence of antiferromagnetic hematite phase ( $\alpha\text{-Fe}_2\text{O}_3$ ) with spinel phase as seen in hematite phase peak in XRD that causes distortion in the unit cell, and additionally, there is shrinkage in the unit cell. Further at  $x = 0.2$ , larger number of  $Co^{2+}$  ions go in site A with small fraction in site B. By virtue of  $Co^{2+}$  ions distribution in site A, unit cell shrinkage is there. Also with the distribution of  $Zn^{2+}$  ions in site B, enlargement in unit cells is occur. Moreover, small fraction of  $Co^{2+}$  ions goes to site B in place of  $Ni^{2+}$  ions and enlarges the unit cell. Also at high doping concentration ( $x = 0.6$ ), the concentration of  $Co^{2+}$  ions has also increase in both the sites that causes the enlargement in unit cell. As a result, D has been increased due to the enlargement of the unit cell [6,7]. The Co-doping effect on d-spacing (d) equation (1.2) and lattice constant (a) equation (1.3), using the following relations:

$$n d \sin \theta = n \lambda \quad (1.2)$$

$$a = d (h^2+k^2+l^2)^{1/2} \quad (1.3)$$

The values of d and a for the thin film as shown in Figures (1.4), (1.5), (1.6), (1.7), (1.8) and (1.9) first decrease from  $x = 0.0$  to  $0.2$  and then increase with Co doping. The distribution of all  $Co^{2+}$  ions in smaller site A and comparable distribution of  $Zn^{2+}$  ions in larger site B that cause the decrease in values at  $x = 0.4$  and also attributed to the presence of hematite phase at this particular composition is the main reason for lattice shrinkage [8,9]. With Co doping at  $x = 0.6$ , all  $Co^{2+}$  ions also distributed in site A and equivalent  $Zn^{2+}$  ions distributed over site B. By virtue of high concentration of  $Co^{2+}$  ions in site A, more lattice shrinkage is there than at  $x = 0.6$ . The increasing values of d and a by means of Co doping (at  $x = 0.8$  and  $1$ ) attribute to the lattice expansion caused by the distribution of  $Co^{2+}$  and  $Zn^{2+}$  ions in both sites. The shift in position of diffraction angle with doping is also correlated with change in D, d and a.

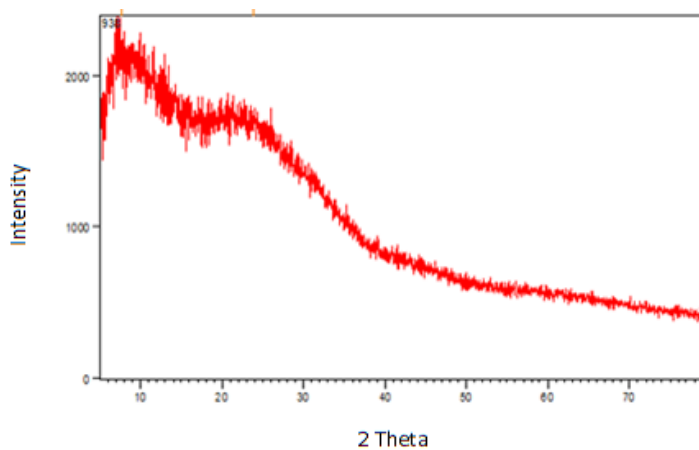
**Fig.4.** The XRD pattern at  $x = 0$  for the thin film analysis.



Peak List:

| Pos.( °2 Th.) | Height(cts) | FWHM Left(°2Th.) | d. spacing(A°) | Rel. Int.(%) |
|---------------|-------------|------------------|----------------|--------------|
| <b>7.6(4)</b> | 405(59)     | 6(1)             | 11.64330       | 100.00       |
| <b>23(1)</b>  | 67(174)     | 8(17)            | 3.82608        | 16.53        |

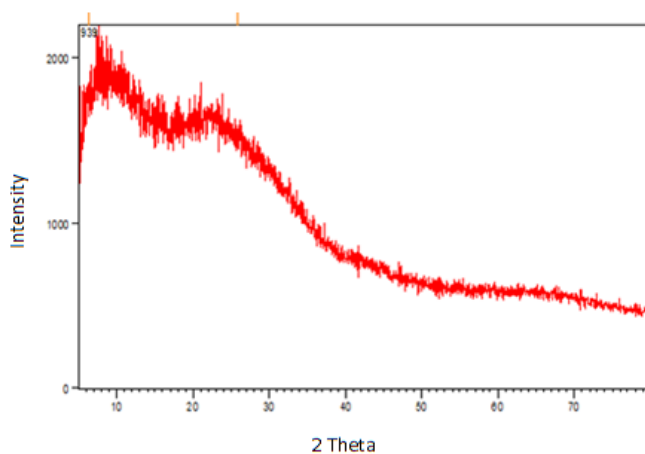
**Fig.5.** The XRD pattern at x = 0.2 for the thin film analysis.



Peak List

| Pos.( °2 Th.) | Height(cts) | FWHM Left(°2Th.) | d. spacing(A°) | Rel. Int.(%) |
|---------------|-------------|------------------|----------------|--------------|
| <b>8(3)</b>   | 204(752)    | 4(11)            | 11.52108       | 100.00       |
| <b>24(1)</b>  | 107(247)    | 7(8)             | 3.71724        | 52.25        |

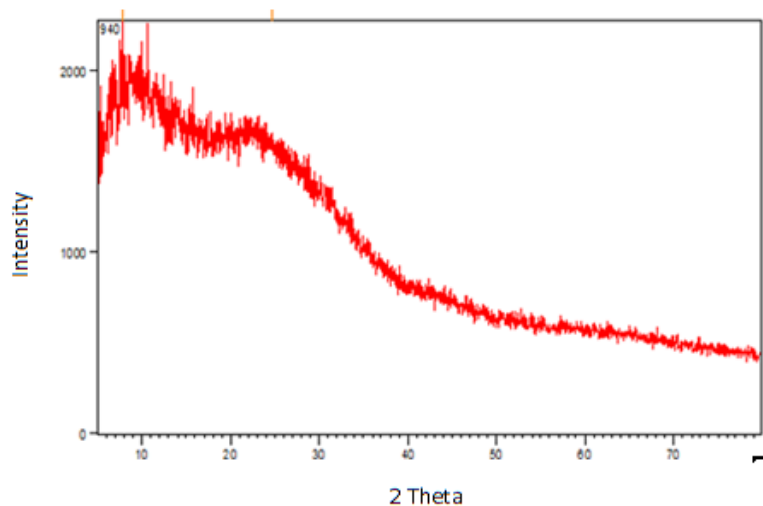
**Fig.6.** The XRD pattern at x = 0.4 for the thin film analysis.



Peak List

| Pos.( °2 Th.) | Height(cts) | FWHM Left(°2Th.) | d. spacing(A°) | Rel. Int.(%) |
|---------------|-------------|------------------|----------------|--------------|
| 6(6)          | 233(1167)   | 6(8)             | 14.12069       | 100.00       |
| 26(1)         | 210(393)    | 14(8)            | 3.43789        | 89.88        |

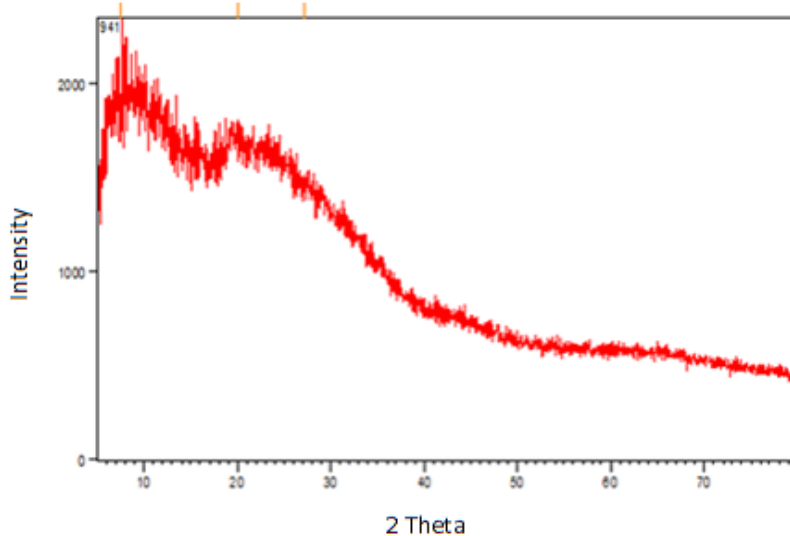
**Fig.7.** The XRD pattern at x = 0.6 for the thin film analysis.



Peak List

| Pos.( °2 Th.) | Height(cts) | FWHM Left(°2Th.) | d. spacing(A°) | Rel. Int.(%) |
|---------------|-------------|------------------|----------------|--------------|
| 8(1)          | 229(199)    | 11(57)           | 11.18824       | 100.00       |
| 25(1)         | 180(89)     | 8(2)             | 3.60397        | 78.77        |

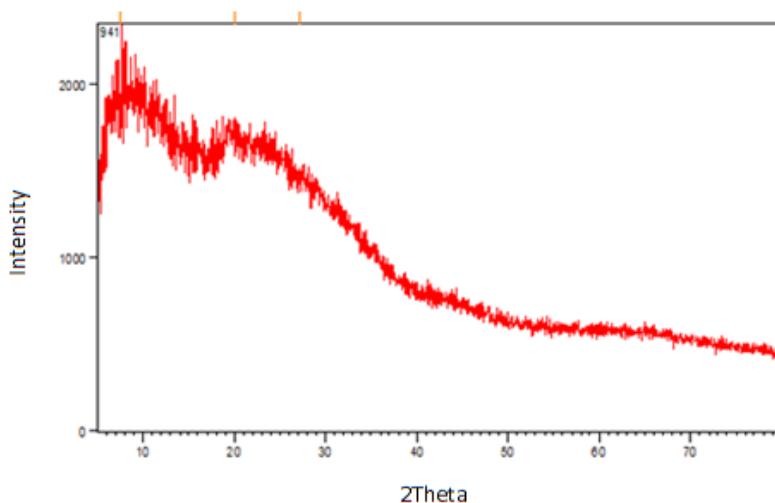
**Fig.8.** The XRD pattern at x = 0.8 for the thin film analysis



Peak List:

| Pos.( °2 Th.) | Height(cts) | FWHM Left(°2Th.) | d. spacing(A°) | Rel. Int.(%) |
|---------------|-------------|------------------|----------------|--------------|
| 8(9)          | 287(1078)   | 7(53)            | 11.64920       | 100.00       |
| 20(2)         | 112(126)    | 3(2)             | 4.42164        | 39.16        |
| 27(11)        | 178(1640)   | 12(90)           | 3.28172        | 61.93        |

**Fig.9.** The XRD pattern at x = 1 for the thin film analysis



Peak List:

| Pos.( °2 Th.) | Height(cts) | FWHM Left(°2Th.) | d. spacing(A°) | Rel. Int.(%) |
|---------------|-------------|------------------|----------------|--------------|
| 8(9)          | 287(1078)   | 7(53)            | 11.64920       | 100.00       |
| 20(2)         | 112(126)    | 3(2)             | 4.42164        | 39.16        |
| 27(11)        | 178(1640)   | 12(90)           | 3.28172        | 61.93        |

**Evaluation of crystallinity**

“Crystalline” means the degree of order within the crystal lattice. A poor crystallinity can be caused by disorder in the crystal (like foreign atoms: carbonate instead of phosphate) or by a small spatial extension of order for small crystals [10].

The crystallinity noted by  $X_c$ , corresponding to the fraction of crystalline sample phases in the investigated volume of powder samples. The  $X_c$ , and the average crystallite size are related structural parameters of materials since both are extracted from the width of a corresponding reflection peak of XRD pattern. The fraction of crystalline phase ( $X_c$  %) in powders can be evaluated by the following equation (1.4) [10 ,11].

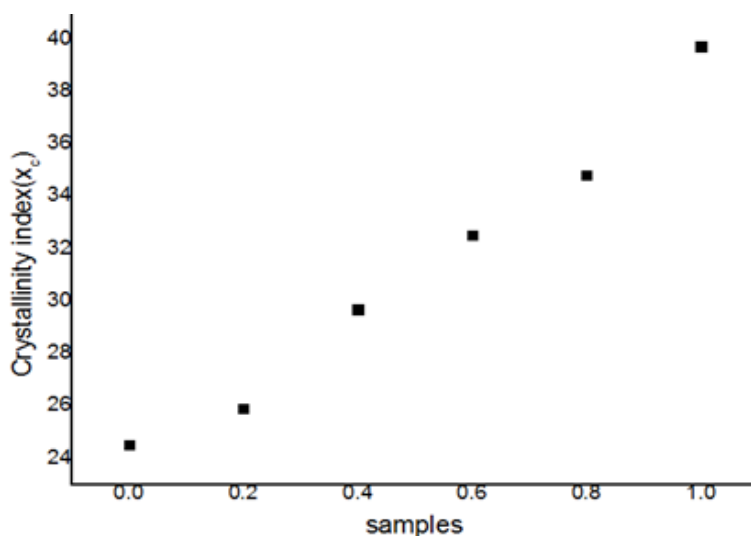
$$X_c = 1 - \left( \frac{V}{I} \right) \quad (1.4)$$

Where  $X_c$ : is the crystallinity degree,  $I$ : is the intensity of the main peak reflection.  $V$ : is the intensity of the hollow between the main peak and the peak beside it.

In the present work it is found that, the degree of crystallinity of the phases is increased as the  $Cr^{3+}$  increased up to 1. Then decreases by add more boron content, as shown in Fig. (1.10).

It is notable that the chromium ions may be able to contact with the network, has the ability to change easily its coordination with oxygen between three and four and hence can form variable structural units in perovskite crystals [11,12]. A second interest comes because chrome has the smallest mass compared to other network forming elements (e.g. Fe). Also, this causes more pores in the structure and increases of site interaction with other elements.

**Fig. 10.** Crystallinity index ( $X_c$ ) of all samples against percentage of chromium oxide



#### Determination of crystallites size of phases by Scherer's equation

The crystallite size was calculated from the broadening in the XRD pattern. According to the Scherer's equation (1.5):

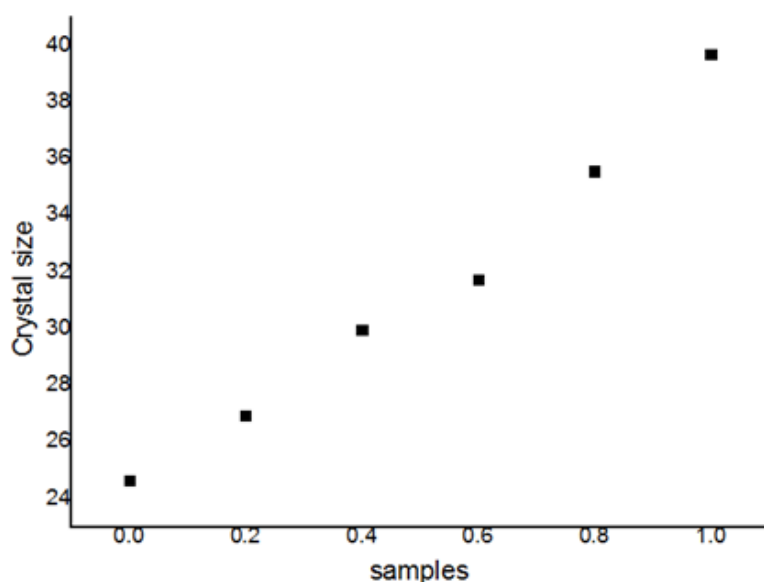
$$D = \frac{k\lambda}{\beta \cos \theta} \quad (1.5)$$

Where  $D$  is the average crystallite size,  $\beta$  is the full width of the peak at half of maximum intensity (rad) (FWHM),  $\lambda$  is the wavelength of monochromatic X-ray beam radiation  $CoK\alpha$  radiation ( $\lambda=1.54056 \text{ \AA}$ ),  $\theta$  is the peak diffraction angle,  $K$  is a Scherer constant defined as the crystallite shape and is approximately equal 0.9.

From Scherer's equation the peak widths, expressed in radians are inverse proportional to the average crystallite size  $D$ . This peak width increases from highly crystalline sample gives rise narrow peaks and poorly crystalline sample gives rise to broad. To determine the full width at half maximum (FWHM) we used three strongest peaks for all investigated perovskite samples. From Scherer's equation the peak widths, expressed in radians are inverse proportional to the average crystallite size  $D$ . This peak width increases from highly crystalline sample gives rise narrow peaks and poorly crystalline sample gives rise to broad.

Fig.(1.11) shows the relation between average crystallites size of apatite formation and the amount of  $\text{Cr}^{3+}$  contents. it notices that, the average crystallites size of the crystalline surface layer of samples increases with increasing the amount of  $\text{Cr}^{3+}$  additives under certain value which called critical concentration (up to 1), where ionic radius of chromium atom ( $\text{Cr}^{3+}$ ) (0.62) smaller than the ionic radius of iron atoms ( $\text{Fe}^{3+}$ ) (0.64) which increase the samples surface area [13,14].

**Fig.11.** The relation between average crystallites size of apatite formation and the amount of  $\text{Cr}^{3+}$  contents.

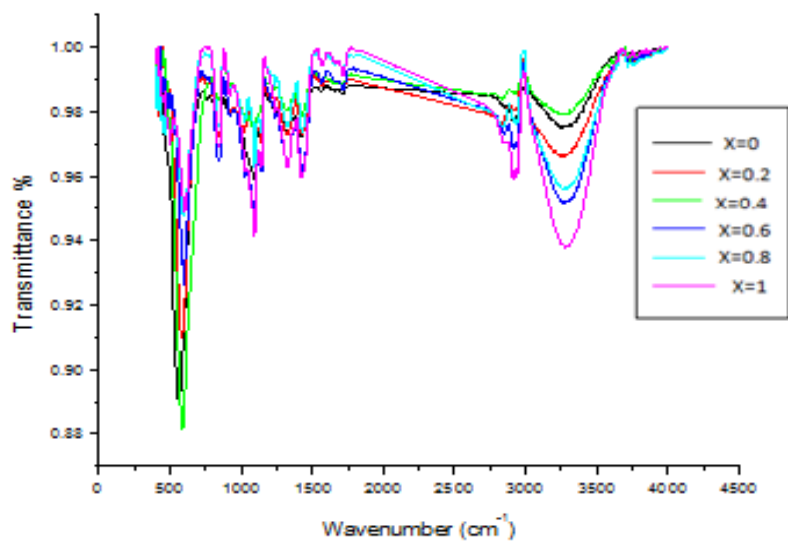


### FTIR Analysis

The FTIR spectra at room temperature used for examine synthesized powder of  $\text{Ni}_{0.6}\text{Zn}_{0.4}\text{Cr}_x\text{Fe}_{2-x}\text{O}_4$ . Absorption peaks for the prepared samples thin film at  $x = 0, 0.2, 0.4, 0.6, 0.8$  and  $1$  are obtained at  $559, 582, 586, 595, 607, 611 \text{ cm}^{-1}$  respectively. The positions of the ions in the crystal through the vibrational modes of a crystal can be studied with the help of an infrared absorption spectrum [15,16]. It is known that the normal cubic spinels have two IR bands representing the fundamental absorption bands. From Figure (1.12) it is observed that there are two main frequency bands, namely, the high frequency band( $\nu_1$ ) is observed at  $529\text{-}549 \text{ cm}^{-1}$  whereas the lower frequency band ( $\nu_2$ ) is observed at  $422\text{-}466 \text{ cm}^{-1}$ . The intensity of the high frequency band( $\nu_1$ ) and frequency band( $\nu_2$ ) appears to increase with the addition of  $\text{Cr}^{3+}$  ions. These two observed frequency bands  $\nu_1$  and  $\nu_2$  are the characteristics of all the ferrite composites and they correspond to the intrinsic vibrations of tetrahedral and octahedral  $\text{Fe}^{3+} - \text{O}_2^{2-}$  complexes, respectively. It explains that the normal mode of vibration of the octahedral cluster is lower than that of the tetrahedral cluster. From FTIR data it is seen that the normal mode of vibration of the tetrahedral cluster ( $529 \text{ cm}^{-1}$ ) is higher than that of the octahedral cluster ( $422 \text{ cm}^{-1}$ ) [17,18]. This can be due to the long bond length of an octahedral cluster than the tetrahedral cluster. This presence of a long shoulder for the A-site is indicative of the presence of other ionic states in that site. By increasing the  $\text{Cr}^{3+}$  content in ferrite powder, the vibrational frequencies  $\nu_1$  and  $\nu_2$  of all the compositions change. Due to the changes in bond lengths  $\text{Fe}^{3+} - \text{O}_2^{2-}$  within octahedral and tetrahedral sites, the difference in frequencies between  $\nu_1$  and  $\nu_2$  is observed. The metal-oxygen vibrational energies increases due to the decrease in the  $\text{Fe}^{3+}_B - \text{O}_2^{2-}$  intermolecular distance,

which arises from the increase of the number of  $\text{Cr}^{3+} - \text{O}_2^{2-}$  complexes caused by the decrease in the number of complexes and the formation of  $\text{Mg}^{2+}/\text{Zn}^{2+} \text{Fe}^{3+} - \text{O}_2^{2-}\text{-Fe}$ . The increasing force constant and shortening of metal-oxygen bonds of the octahedral unit is attributed to the increase in vibrational frequency ( $\nu_2$ ) with an increase in  $\text{Cr}^{3+}$  content in ferrite material. The force constant is the second derivative of the potential energy concerning the site radius with the other independent parameters kept constant. The force constant for the octahedral site(KO) and tetrahedral site(Kt) were calculated by employing the Waldron method [19,20].

**Fig.12.** FTIR spectra of all thin film samples



### Electrical Properties

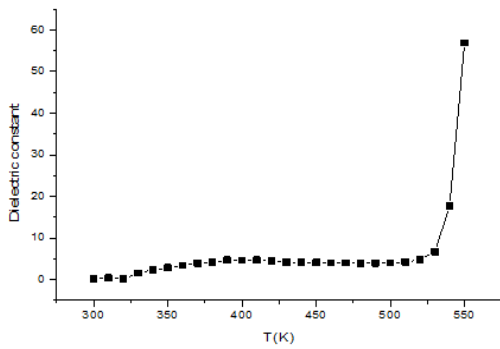
Electrical properties include dielectric loss tangent, dielectric constant, or electrical resistivity, which largely depend on size, shape, crystallinity, porosity, and chemical composition of ferrites.

The dielectric properties are associated with the electric field distribution within the crystal. The dielectric constant was expressed in real and imaginary parts as mentioned in the following equation[21,22]:

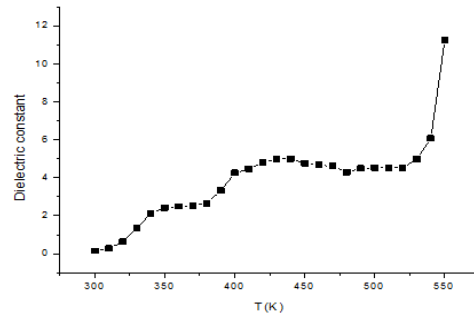
$$\epsilon = \epsilon' - j\epsilon'' \quad (1.6)$$

The real dielectric part gives information about the stored energy. The imaginary part contributes to energy dissipation in the applied AC field. The experimental result demonstrates that the imaginary part of the dielectric constant is more pronounced in comparison to the real part [23,24]. Impedance spectroscopy associates the material's dielectric properties with its microstructures. It also helps in analyzing the influence of various factors such as interfaces, grains, or grain boundaries of polycrystalline materials. The impedance measurements (IM) give us statistics regarding resistive and reactive constituents. The dielectric constant for the thin film of prepared samples is gradually increases with temperature as shown in Figure (1.13a, e and f). It is observed in Figure(1.13b and c) value dielectric constant is beginning arises at 530k° and Figure (1.13d) at 510k°.

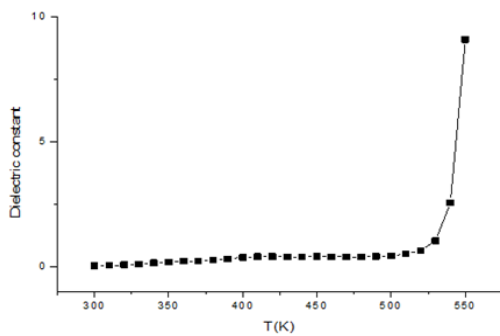
**Fig.13.** Represent dielectric constant with T of all thin film samples.



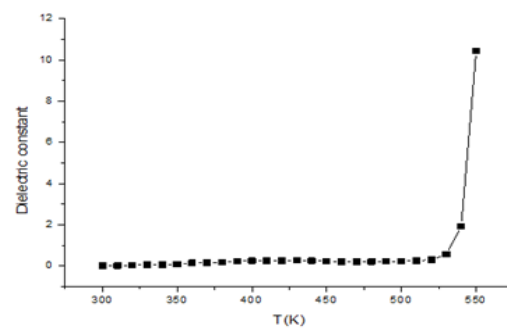
b) x = 0.2



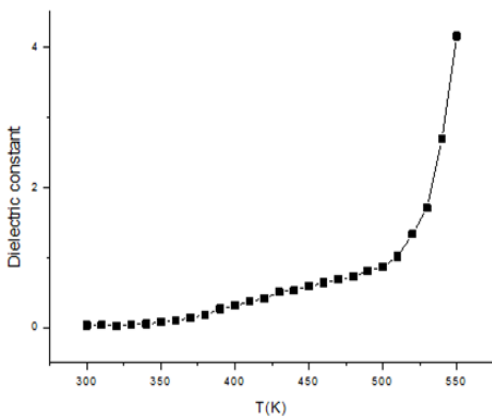
a) x = 0



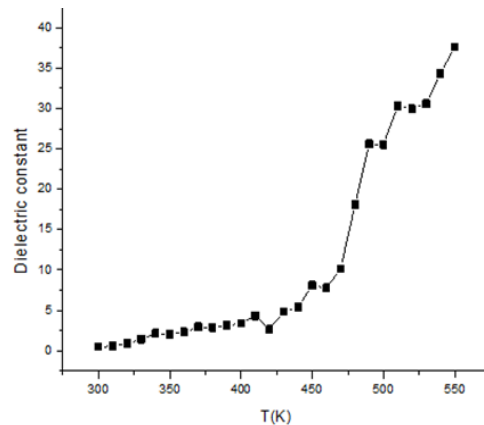
d) x = 0.6



c) x = 0.4



f) x = 1

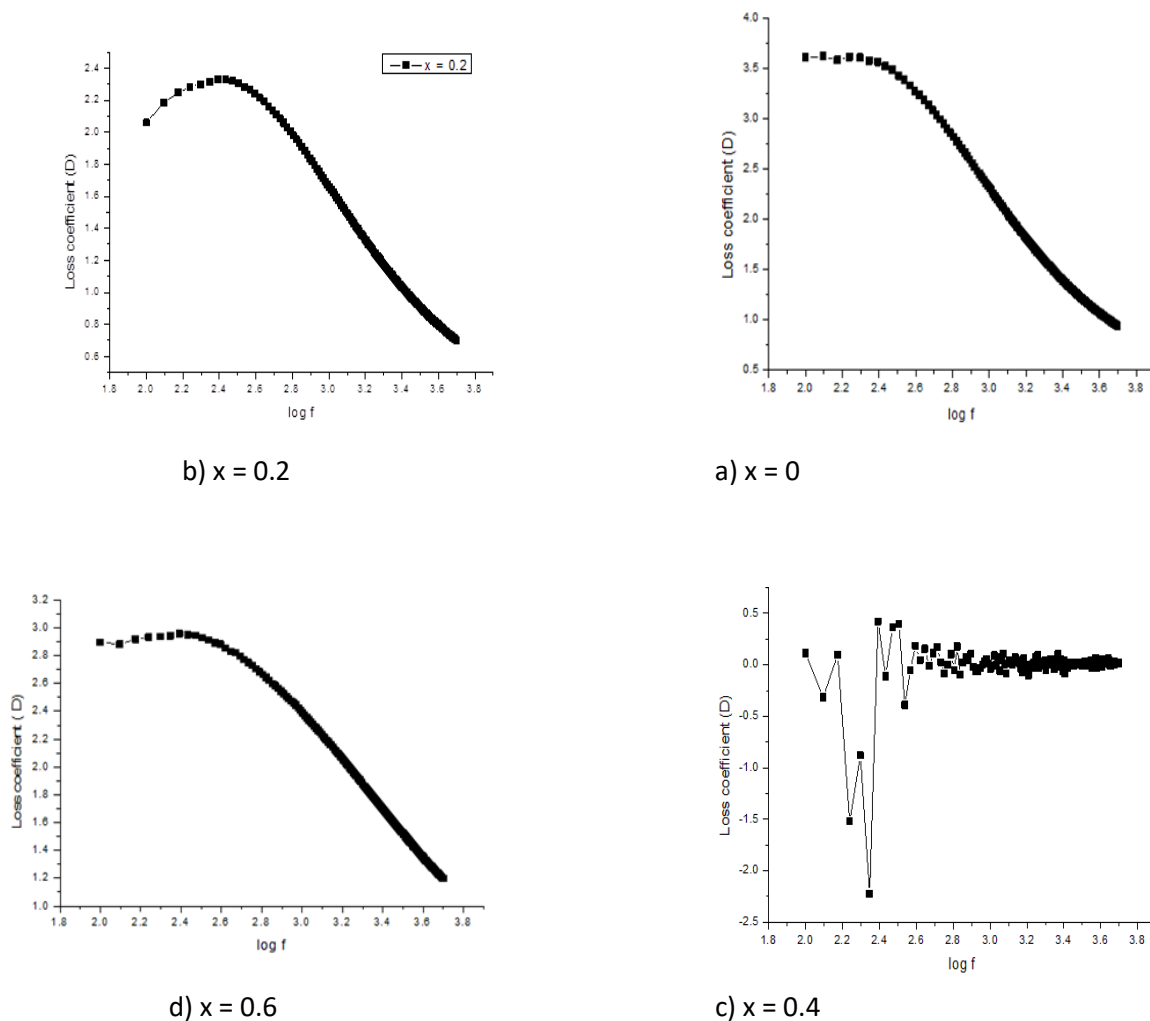


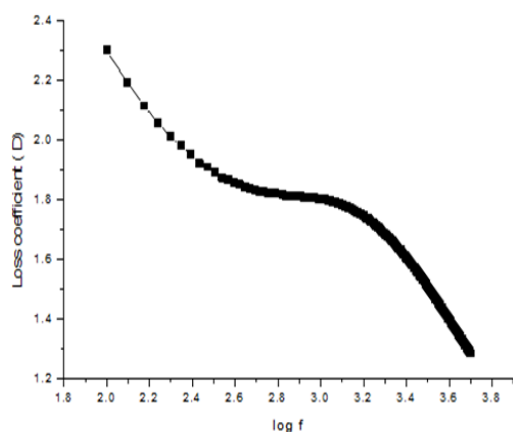
e) x = 0.8

The dielectric loss tangent explains the energy declines within the ferrite. The polarization lags behind the applied alternating field, when the dielectric loss tangent rises. Figure (1.14) represent the graph of dielectric loss varying with frequency. The experimental result demonstrates that in all our synthesized samples in the lower frequency region, the dielectric loss factor is high. The dielectric loss is related to grain boundaries. The high dielectric loss is because of higher resistance due to the existence of grain boundaries. It requires efficient energy for electron transfer between  $Fe^{+2}/Fe^{+3}$  ions, which causes a high loss at a low-frequency region. However, at high-frequency regions, the resistivity declines due to grains. Small energy is needed at octahedral sites for

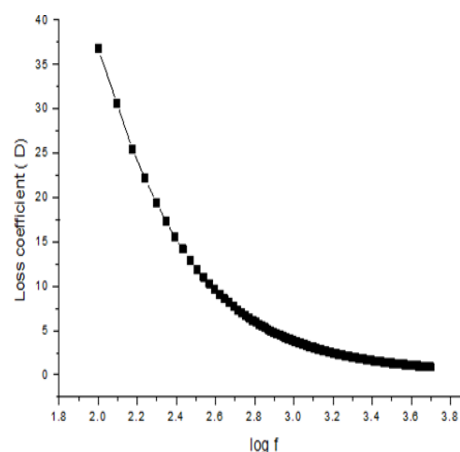
electron transference mechanism between the two iron ions. The high dielectric loss at lower frequencies is due to different factors including impurities, crystal defects, moisture, and inhomogeneity. The thin film exhibits a low dielectric loss as well as excellent frequency. Loss coefficient for the thin film of prepared samples is decreases with frequency increasing except  $x = 0.4$  that is behavior of curve is different. Loss coefficient have peaks at - 0.315, -1.52, -2.225, - 0.11 and - 0.39 . The value less of loss coefficient is – 2.225.

**Fig.14.** Represent loss coefficient with frequency of all thin film samples.





f) x = 1



e) x = 0.8

## Conclusion

The d - spacing (d) and lattice constant (a) decrease from x = 0 to 0.2 and then increase with Co doping. The distribution of all Co<sup>2+</sup> ions in smaller site A and comparable distribution of Zn<sup>2+</sup> ions in larger site B that cause the decrease in values at x = 0.4 and also attributed to the presence of hematite phase at this particular composition is the main reason for lattice shrinkage.

The increasing values of d and a by means of Co doping (at x = 0.8 and 1) attribute to the lattice expansion caused by the distribution of Co<sup>2+</sup> and Zn<sup>2+</sup> ions in both sites. The shift in position of diffraction angle with doping is also correlated with change in D, d and a. The intensity of the high frequency band (v1) and frequency band (v2) appears initially increasing and decrease with 2θ in all of the thin film samples. The behavior of intensity with 2θ is constant at x = 0.8 and 1. From FTIR data it is seen that the normal mode of vibration of the tetrahedral cluster (529cm<sup>-1</sup>) is higher than that of the octahedral cluster (422cm<sup>-1</sup>) and this can be due to the long bond length of an octahedral cluster than the tetrahedral cluster. The dielectric constant is increasing gradually with temperature increased at x = 0, 0.8 and 1. The value of dielectric constant is beginning arises for x = 0.2 and 0.4 at 530ko and for x = 0.6 at 510ko. Loss coefficient is decreases with increase frequency in all the thin film samples except x = 0.4 .

## References

- 1 - Mahalakshmi, S., Srinivasa Manja, K., Nithiyantham, S.: Electrical properties of nanophase ferrites doped with rare earth ions. *J. Supercond. Novel Magn.* 27, 2083–2088 (2014).
- 2 - Iqbal, M.J., Ahmad, Z., Meydan, T., Melikhov, Y.: Physical, electrical and magnetic properties of nano-sized Co–Cr substituted magnesium ferrites. *J. Appl. Phys.* 111, 033906 (2012).
- 3 - Jadhav, S.S., Gore, S., Patange, S., Shirsath, S.: Effect of Cr ions on physical properties of Cu–Zn ferrite nano-particles. *Inter. J. Basic Appl. Res.* 78–81 (2012).
- 4 - Rezlescu E, Sachelarie L, Popa PD, Rezlescu N (2000) Effect of substitution of divalent ions on the electrical and magnetic properties of Ni–Zn–Me ferrites. *IEEE Trans Magn* 36:3962–3967.

5 - George M, Nair SS, John AM, Joy PA, Anantharaman MR (2006) Structural, magnetic and electrical properties of the sol– gel prepared  $\text{Li}_0.5\text{Fe}_2.5\text{O}_4$  fine particles. *J Phys D Appl Phys* 39:900–910.

6 - Hashim, M., Shirsath, S.E., Kumar, S., Kumar, R., Roy, A.S., Shah, J., Kotnala, R.: Preparation and characterization chemistry of nano-crystalline Ni–Cu–Zn ferrite. *J. Alloys Compd.* 549, 348–357 (2013).

7 - Sutka, A., Mezinskis, G., Pludons, A., Lagzdina, S.: Characterization of solgel auto-combustion derived spinel ferrite nanomaterials. *Power Eng.* 56, 254–259 (2010).

8 - El-Sayed, A.: Effect of chromium substitutions on some properties of NiZn ferrites. *Ceram. Int.* 28, 651–655 (2002).

9 - Masti, S., Sharma, A., Vasambekar, P., Vaingankar, A.: Influence of  $\text{Cd}^{2+}$  and  $\text{Cr}^{3+}$  substitutions on the magnetization and permeability of magnesium ferrites. *J. Magn. Mater.* 305, 436–439 (2006) *J Nanostruct Chem* (2015) 5:365–373 373 123.

10 - The effectiveness of bone char in the defluoridation of water in relation to its crystallinity, carbon content and dissolution pattern vol.39, Issue 9, September 1994, pages 807 – 816.

11 - Influence of temperature, ripening time and calcination on the morphology and crystallinity of hydroxyapatite nano particles. Vol.23, Issue10, September 2003, pages 1697 – 1704.

12 - Dynamic structure factor of non crystalline and crystalline systems as revealed by MARI, a neutron chopper instrument vol.71- 72, September, 1997, pages 209 – 232.

13 - Raman investigation of nano sized  $\text{TiO}_2$ : effect of crystallite size and quantum confinement vol. 116, Issue15, March 2012, pages 8792 – 8797.

14 - M.J. Iqbal , M.R. Siddiquah , *J. of Magnetism and Magnetic Materials* 320 (2008) 845 – 850 .

15- Mohammed KA, Al-Rawas AD, Gismelseed AM, Sellai A, Widatallah HM, Yousif A, Elzain ME, Shongwe M (2012) Infrared and structural studies of  $\text{Mg}_{1-x}\text{Zn}_x\text{Fe}_2\text{O}_4$  ferrites. *Phys B Condens Matter* 407:795–804.

16 -Structural and Electrical Properties of Li–Ni Nanoferrites Synthesised by Citrate Gel Auto combustion Method, G. Aravind, D. Ravinder, and V. Nathaniel, *Physics Research International*, Volume 2014, Article ID 672739, page 11.

17 - Magnetic study of nanocrystalline Mg-doped lithium ferrite, Marek Pekala, Frank J. Berry, Hisham M Widatallah, *Czechoslovak Journal of Physics*, 52 (2002) 101-104.

18 - One-Pot Low Temperature Synthesis and Characterization Studies of Nanocrystalline  $\alpha$ -Fe<sub>2</sub>O<sub>3</sub> Based Dye Sensitized Solar Cells, A. Manikandan, A. Saravanan, S. Arul Antony, and M. Bououdina, Journal of Nanoscience and Nanotechnology, 15 (2015) 4358–4366.

19 - - Enhanced Catalytic Activity and Magnetic Properties of Spinel Mn<sub>x</sub>Zn<sub>1-x</sub>Fe<sub>2</sub>O<sub>4</sub> (0.0 ≤ x ≤ 1.0) Nano-Photocatalysts by Microwave Irradiation Route, G. Padmapriya, A. Manikandan, V. Krishnasamy, Saravana Kumar Jaganathan, S. Arul Antony, Journal of Superconductivity and Novel Magnetism, 29(2016) 8-16.

20 - S.Chikazumi, S.Charap, Physics of Magnetism, John Wiley & Sons, NewYork,1964. (pp.153).

21 - Bahadur, D., Rajakumar, S., Kumar, A.: Influence of fuel ratios on auto combustion synthesis of barium ferrite nano particles. J. Chem. Sci. 118, 15–21 (2006).

22 - Jadhav, S.S., Gore, S., Patange, S., Shirsath, S.: Effect of Cr ions on physical properties of Cu–Zn ferrite nano-particles. Inter. J. Basic Appl. Res. 78–81 (2012).

23 - Rezlescu E, Sachelarie L, Popa PD, Rezlescu N (2000) Effect of substitution of divalent ions on the electrical and magnetic properties of Ni–Zn–Me ferrites. IEEE Trans Magn 36:3962–3967.

24 - George M, Nair SS, John AM, Joy PA, Anantharaman MR (2006) Structural, magnetic and electrical properties of the sol– gel prepared Li<sub>0.5</sub>Fe<sub>2.5</sub>O<sub>4</sub> fine particles. J Phys D Appl Phys 39:900–910.